

---

# Dual Data Alignment Makes AI-Generated Image Detector Easier Generalizable

---

Ruoxin Chen<sup>1</sup>, Junwei Xi<sup>2</sup>, Zhiyuan Yan<sup>3</sup>, Ke-Yue Zhang<sup>1</sup>, Shuang Wu<sup>1</sup>,  
Jingyi Xie<sup>4</sup>, Xu Chen<sup>2</sup>, Lei Xu<sup>5</sup>, Isabel Guan<sup>6</sup>, Taiping Yao<sup>1</sup>, Shouhong Ding<sup>1</sup>  
cusmochen@tencent.com

## Abstract

The rapid increase in AI-generated images (AIGIs) underscores the urgent need for generalizable detection methods. Existing detectors, however, are often trained on biased datasets, leading to the possibility of overfitting on non-causal image attributes that are spuriously correlated with real/synthetic labels. While these biased features enhance performance on the training data, they result in substantial performance degradation when applied to unbiased datasets. One common solution is to perform dataset alignment through generative reconstruction, matching the semantic content between real and synthetic images. However, we revisit this approach and show that pixel-level alignment alone is insufficient — the reconstructed images still suffer from frequency-level misalignment, which can perpetuate spurious correlations. To illustrate, we observe that reconstruction models tend to restore the high-frequency details lost in real images (possibly due to JPEG compression), inadvertently creating a frequency-level misalignment, where synthetic images appear to have richer high-frequency content than real ones. This misalignment leads to models associating high-frequency features with synthetic labels, further reinforcing biased cues. To resolve this, we propose Dual Data Alignment (DDA), which aligns both the pixel and frequency domains. DDA generates synthetic images that closely resemble real ones by fusing real and synthetic image pairs in both domains, enhancing the detector’s ability to identify forgeries without relying on biased features. Moreover, we introduce two new test sets: DDA-COCO, containing DDA-aligned synthetic images for testing detector performance on the most aligned dataset, and EvalGEN, featuring the latest generative models for assessing detectors under new generative architectures such as visual auto-regressive generators. Finally, our extensive evaluations demonstrate that a detector trained exclusively on DDA-aligned MSCOCO could improve across 8 diverse benchmarks by a non-trivial margin, showing a +7.2% on in-the-wild benchmarks, highlighting the improved generalizability of unbiased detectors. Our code is available at: <https://github.com/roy-ch/Dual-Data-Alignment>.

## 1 Introduction

The rise of AI-generated images (AIGIs) poses significant risks to digital security, including the potential for misinformation, fraud, and copyright violations [11, 18, 19, 16, 28, 40, 38, 37]. This severe security issue underscores the urgent need for reliable detection methods to differentiate synthetic images from authentic ones. Despite advances in AIGI detection techniques [4, 26, 29], the rapid evolution of generative models and the emergence of new architectures present cross-domain generalization challenges. This is especially evident in zero-shot scenarios involving previously unseen generation paradigms.

---

<sup>1</sup> Tencent YouTu Lab, <sup>2</sup> East China University of Science and Technology, <sup>3</sup> Peking University, <sup>4</sup> Renmin University of China, <sup>5</sup> Shenzhen University, <sup>6</sup> Hong Kong University of Science and Technology

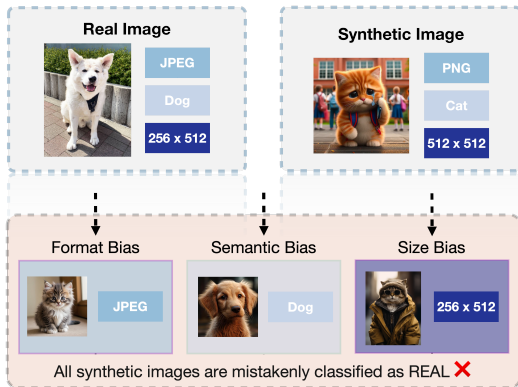


Figure 1: **Illustration of dataset bias.** Top row: Real and synthetic images may show disparities in format, content, and size. Real images are typically in JPEG format, with varying sizes and centered semantics. Bottom row: Detectors trained on datasets containing these discrepancies are prone to learning biased features, incorrectly associating authenticity with format, image size, or semantics. This leads to an inability to detect synthetic images that resemble real training data in specific characteristics.

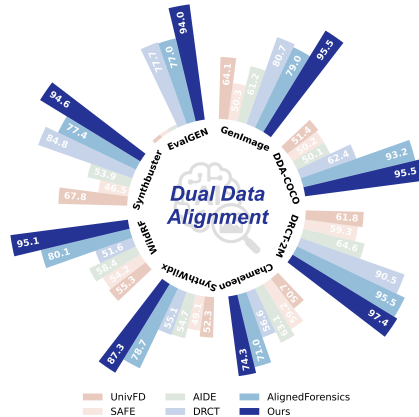


Figure 2: **Overall average balanced accuracy comparison between detection methods on eight different test sets.** Our model is exclusively trained on MSCOCO real images with DDA alignment. The consistent outperformance of DDA on three in-the-wild (Chameleon, WildRF, and SynthWildx) and five manually-crafted datasets validates the generalizability. Detailed settings and results are provided in Section 4, which also demonstrate that DDA exhibits lower cross-dataset performance fluctuations.

The generalizability of AIGI detectors is hindered by dataset biases [12, 4, 27, 13]. Existing datasets often exhibit systematic discrepancies in attributes unrelated to the authority. Works [31] illustrate semantic bias through word frequency analysis, and studies [29] demonstrate image size bias by analyzing six datasets where synthetic images are uniformly sized as multiples of  $128 \times 128$ . These non-causal features could be exploited by models to distinguish real from synthetic images, resulting in biased detector performance that fails to generalize across different datasets. Figure 1 visually illustrates such bias. **Dataset alignment holds promise in addressing the issue of dataset bias** by ensuring synthetic images closely resemble real ones, *excluding authenticity-related factors and directing detectors to focus on forgery-related cues*. Specifically, studies [12] reveal systematic discrepancies in format and size biases: real images are JPEG-encoded and vary in size, whereas synthetic images are uniformly PNG-encoded and fixed in size. SemGIR [39], DRCT [4], B-Free [13] aim to mitigate content discrepancies using diffusion reconstruction techniques that generate images semantically similar to real ones. Works [14, 41] prevent models from learning semantics-dependent features by breaking images into patches and shuffling them.

However, in this paper, we ask: *Does reconstruction truly eliminate the potential misalignment and bias?* Our answer is NO, as we found that although reconstruction-based methods align datasets at the pixel level, they still **introduce subtle misalignments at the frequency level**. Specifically, generative alignment methods, including generative reconstruction, provide detailed information across all frequency bands. In particular, the reconstructed images restore high-frequency components that are typically diminished in real images, possibly due to compression during transmission or storage. Consequently, **synthetic images exhibit prominent high-frequency details, while real images show only minor**, creating a noticeable disparity in the quantity of high-frequency components, rather than in the actual high-frequency content itself. This spurious correlation can cause the model learned to learn such a bias could mistakenly recognize.

In this paper, we propose **Dual Data Alignment (DDA)**, an effective technique that aligns synthetic images with real ones across both pixel and frequency domains. DDA consists of three steps: 1) VAE reconstruction for pixel alignment, 2) high-frequency fusion to eliminate bias, and 3) pixel mixup for further alignment in the pixel domain. As shown in Figure 2, **a single model trained on DDA-aligned MSCOCO demonstrates significant improvements across benchmarks: +12.4%**

Table 1: Comparing on dataset alignment.

Domain	UnivFD [26]	C2P-CLIP [31]	SAFE [21]	AIDE [36]	DRCT [4]	AlignedForensics [27]	Ours
Frequency	Low	Low	Low	Low	Low	Low	High
Pixel	Low	Low	Low	Low	Medium	High	High

Syn.1	Syn.2	Syn.3	Aligned Syn.	Real
PNG Dog 512 x 512	JPEG Cat 256 x 512	PNG Dog 512 x 512	JPEG Dog 256 x 512	JPEG Dog 256 x 512

Figure 3: Visual illustration of how dataset bias affects decision boundaries in synthetic image detection. **Left:** Detectors trained on biased datasets—where synthetic images (e.g., Syn.1–3) differ from real images in format, content, or resolution—tend to learn spurious decision boundaries. These boundaries may misclassify samples that deviate from the biased training distribution. **Right:** When synthetic images are carefully aligned with real images across multiple domains (e.g., format, content, resolution), the model learns a tighter, more generalizable decision boundary. This alignment enables better detection of previously unseen synthetic images by covering a wider distributional range.

on GenImage <sup>1</sup>, +9.8% on Synthbuster and +17.7% on EvalGEN, with significantly lower fluctuations across subset evaluation performance – usually 1/3 to 2/3 that of the SoTA detectors – suggesting that DDA learns a reliable and general feature. Moreover, we introduce two new evaluation datasets: 1. DDA-COCO, a test set consisting of real images from MS COCO and their DDA-aligned counterparts, which are mostly aligned. Evaluation results show that prior detectors suffer significant performance drops on DDA-COCO, further validating the alignment quality of the DDA method. 2. EvalGEN, a test set consisting of FLUX, GoT, Infinity, NOVA, and OmniGen, which includes both advanced auto-regressive and diffusion generators, serving for measuring detectors’ generalizability under newly evolved generative models.

## 2 Related Works

**AIGI Detection.** CNNSpot [34] trains a vanilla CNN model to detect AIGI, finding that detectors easily recognize synthetic images from seen models but struggle to generalize to unseen ones. UnivFD [26] employs CLIP as the detector backbone, showing the improvements in generalizability in detecting unseen generators with pretrained models. Subsequent works [25, 31, 41] explore model architectures and image preprocessing for more generalizable AIGI detection. C2P-CLIP enhances the pretrained CLIP backbone for AIGI detection by injecting ‘real’ and ‘fake’ concepts. Works [32, 5, 21, 17] exploit frequency domain artifacts, showing that frequency artifacts could well discriminate. NPR [33] explores the upsampling artifact in generative models. However, these methods’ generalizability is limited by either content bias or frequency-level bias, with a significant chance of exploiting non-causal features like image format, which can significantly degrade performance on unbiased test sets.

**Dataset alignment.** The evaluation bias issue in AIGI detection is firstly introduced in the work [12], showing that image format and size are common biases unintentionally exploited by detectors. FakeInversion [3] introduces a bias-reduced evaluation benchmark, mitigating thematic and stylistic biases by collecting synthetic images that match real images in both content and style. A line of subsequent works explores eliminating bias in the training set to enhance generalizability. SemGIR [39] regenerates synthetic images by semantic-level reconstruction conditioned on the real counterpart’s description, aiming to better align synthetic and real images semantically. DRCT [4] employs diffusion reconstruction for improved semantic alignment. B-Free [13] addresses dataset bias through self-conditioned inpainted reconstructions and content augmentation. However, this inpainting paradigm can alter the center object, corrupting the semantic alignment. AlignedForensics [27] performs simple VAE reconstruction without latent space manipulation, resulting in synthetic images that closely match real images in semantics and resolution. However, both B-Free and AlignedForensics overlook format alignment, creating space for JPEG-based shortcuts in discrimination. These methods are summarized in Table 1.

<sup>1</sup>In the test, we use JPEG-aligned GenImage, where synthetic images are compressed with a JPEG quality factor of 96, matching the format of real images. This approach helps mitigate format bias-based discrimination.

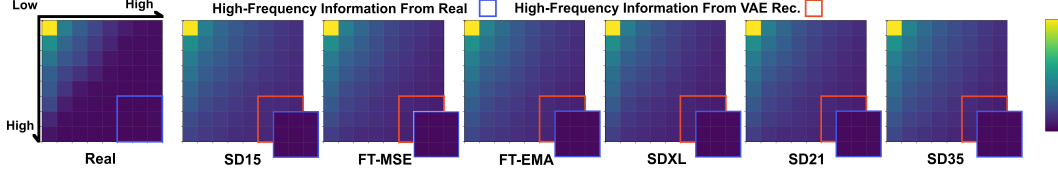


Figure 4: **Visualization of frequency domain energy using 2D Discrete Cosine Transform (DCT).** The left column shows a real image, while the remaining columns display images reconstructed by VAEs from various Stable Diffusion models. The grids represent frequency components, with the top-left and bottom-right indicating low- and high-frequency regions, respectively. Lighter areas correspond to higher energy. Notably, real images exhibit significantly darker high-frequency regions compared to VAE reconstructions, indicating weaker high-frequency content in real images and rich high-frequency signals in synthetic ones.

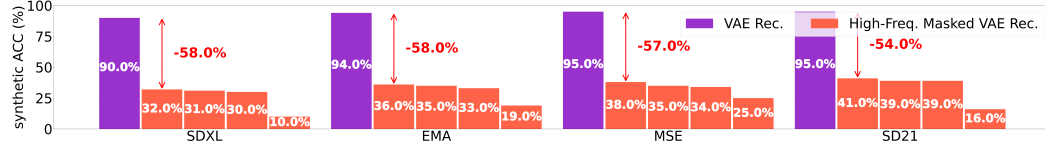


Figure 5: **Evidence for the existence of biased frequency-based features to discriminate reconstructed images.** We apply a binary mask to the DCT coefficients, systematically nullifying high-frequency components where either the horizontal or vertical frequencies exceeded 95%, 90%, 85% and 80% of their respective spectral ranges to generate High-Freq. Masked VAE Rec.

### 3 Methodology

#### 3.1 Motivation and Analysis

**Misaligned Dataset.** In the absence of additional supervision, detectors must rely exclusively on the training set to learn the concept of ‘real’ versus ‘synthetic’. When these two classes differ systematically in non-causal attributes—such as image size, compression format, or semantic content—the model may incorrectly learn to associate these irrelevant features with authenticity. These spurious signals are often more salient than subtle, genuine artifacts that actually distinguish real from synthetic images, making it more difficult for the model to learn truly generalizable, causally relevant features. Figure 3 illustrates how such biases constrain the learned decision boundary, as shown in the left three panels. In contrast, the rightmost panel shows that when synthetic images are carefully aligned with real images across key domains, the model can learn a tighter, more transferable decision boundary, improving generalizability to unseen data.

**Reconstruction-based Alignment.** To align synthetic images with real ones, some approaches [39, 42, 13] employ txt2img generative models to generate images with similar semantic content, conditioned on the image label or image captions obtained through pretrained models. However, images generated using this approach often differ from the originals due to the lack of strong and detailed supervision, which prevents the generated images from fully matching the original images in all semantic details. DRCT [4, 13] leverages Img2Img diffusion reconstruction, directly using the image itself to guide the reconstruction of a real image  $x$  into a synthetic counterpart  $\hat{x}$  as follows:

$$\hat{x} = \text{Decoder}(\hat{z}), \quad \text{where} \quad \hat{z} = z + \epsilon_t - \epsilon_\theta(z, t), \quad z = \text{Encoder}(x) \quad (1)$$

where  $z$  represents the encoded latent of the real image, while  $\hat{z}$  is modified by adding noise and subsequently denoising, creating new latents that subtly differ from  $z$ . However, such self-supervised diffusion reconstruction can still lead to changes in image details due to modifications in the latent space, which is responsible for the generation of semantics. The work [27] further simplifies the reconstruction process by using a Variational Autoencoder (VAE)—a submodule used in all stable diffusion generators—without any modification to the latent. This approach generates images that closely match the original real image at the pixel level.

$$\hat{x} = \text{Decoder}(z), \quad \text{where} \quad z = \text{Encoder}(x) \quad (2)$$

**Frequency-Level Misalignment Exists and Can Be Exploited.** Frequency-domain analysis has been widely explored in AIGI detectors [30, 21, 24, 36], demonstrating that frequency information is a crucial feature for AIGI detection. This motivates us to revisit the alignment of synthetic images in the frequency domain. Surprisingly, despite pixel-level alignment, synthetic counterparts exhibit significant discrepancies in high-frequency content. Figure 4 visualizes this discrepancy between

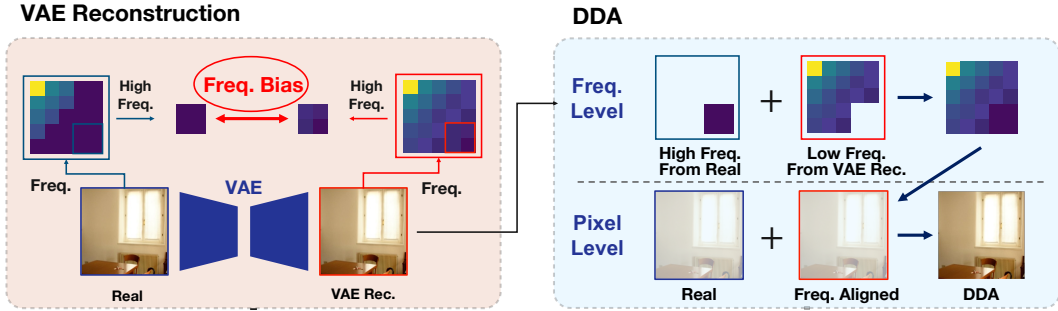


Figure 6: DDA pipeline. **Left:** VAE-reconstructed images differ from real ones in the intensity of high-frequency components. **Right:** DDA fuses high-frequency information from real images into the VAE-reconstructed images to align them in the frequency domain. Then, DDA uses pixel-level mixup of real and frequency-aligned images to further align them in the pixel domain.

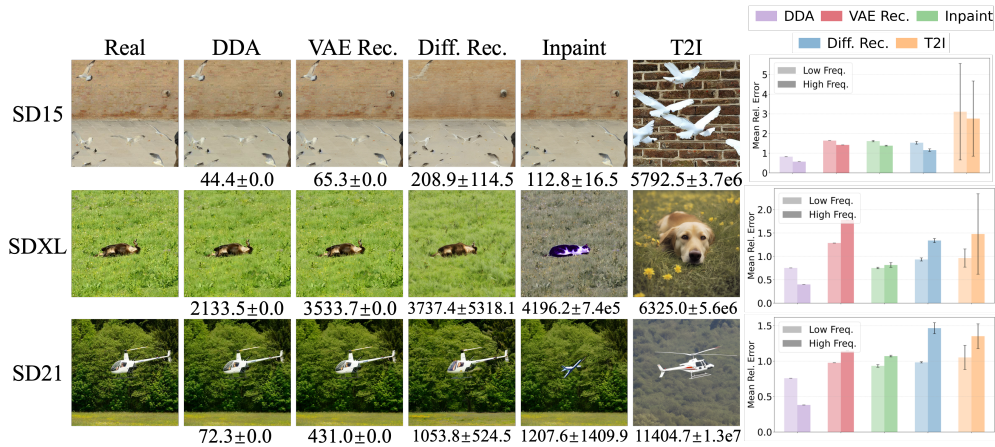


Figure 7: Comparison of various image processing methods based on loss with respect to the real image. **Left:** Comparison of image processing methods across three Stable Diffusion model series (SD15, SDXL, SD21) displaying real images alongside processed versions using DDA, VAE reconstruction (VAE Rec.), diffusion reconstruction (Diff. Rec.), masked inpainting with prompts (Inpaint), and text-to-image generation (T2I). Mean squared error (MSE) values relative to the real image are presented beneath each processed image, and each mse value is calculated by generating 100 images. **Right:** Visualization of relative error metrics for each processing method across the same model series, segregated into low frequency and high frequency bands as calculated using discrete Fourier transform (DFT). Bar charts illustrate comparative error magnitudes across different reconstruction techniques and frequency components. Both pixel-level and frequency-level analyses indicate that DDA produces synthetic images most similar to the real images.

the real image and synthetic images reconstructed using various VAEs. Real images are often with relatively poor high-frequency information, which likely due to operations such as JPEG compression removing high-frequency details like sharp edges and fine textures, elements less noticeable to the human eye. Having identified this frequency-level discrepancy, another question arises: "Can this disparity be leveraged, or are we overestimating its impact?" To evaluate its effect, we assess the impact of high-frequency information by measuring the variance in detector performance on VAE-reconstructed images. As shown in Figure 5, the empirical results are surprising: visually identical VAE-reconstructed images are easily detected by the frequency-based SAFE detector [21], with a detection rate of 93%, suggesting an evident difference in the frequency domain. However, when we mask high-frequency information minimally, the detection rate significantly drops. This substantial drop is unlikely to be solely attributed to information loss, but rather suggests that detectors may be exploiting biased features, specifically the presence of richer high-frequency details in synthetic images. In conclusion, we expose the frequency-level discrepancy between real and synthetic images, demonstrating that this misalignment can be exploited by certain detectors.

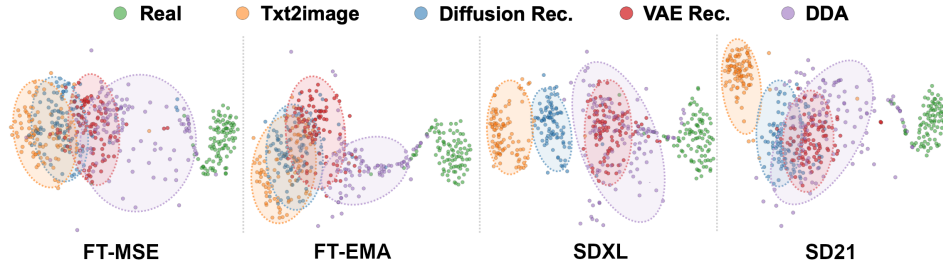


Figure 8: t-SNE visualizations comparing real and generated images, illustrating the proximity of synthetic image cluster centers to real images in feature space. The ordering of proximity—from closest to farthest—is: DDA, VAE reconstruction, diffusion reconstruction, and text-to-image (T2I) generation. These results indicate that DDA produces synthetic samples most closely aligned with real images near the data manifold boundary, thereby facilitating the learning of a tighter and more generalizable decision boundary.

### 3.2 Dual Data Alignment

Motivated by the previous observation, we propose DDA, a technique that generates synthetic images aligned with real ones in both the pixel and frequency domains to mitigate the learning of biased features. As illustrated in Figure 6, DDA consists of three steps: 1) **VAE Reconstruction**: Generate pixel-wise similar images containing VAE-specific artifacts. 2) **Frequency-Level Alignment**: Fuse high-frequency components from real images into the VAE-reconstructed images to eliminate discrepancies in the frequency domain. Specifically, we replace the 2D-DCT coefficients whose horizontal or vertical frequencies exceed a predefined threshold  $T_{freq}$  with those from the corresponding real image. 3) **Pixel-Level Alignment**: Apply mixup between real and frequency-aligned images to ensure pixel-domain alignment. Concretely, we generate a closely aligned synthetic image as follow:

$$x_{\text{mix}} = r_{\text{pixel}} \cdot x_{\text{real}} + (1 - r_{\text{pixel}}) \cdot x_{\text{syn}} \quad (3)$$

where  $r_{\text{pixel}} \in [0, 1]$  controls the degree of pixel-level alignment. A higher  $r_{\text{pixel}}$  value yields a closer synthetic image in the pixel space. In practice,  $r_{\text{pixel}}$  is sampled from a uniform distribution  $\mathcal{U}(0, R_{\text{pixel}})$ . A higher  $r_{\text{pixel}}$  value results in a synthetic image that more closely resembles the real image in pixel space. Together, these steps ensure that the resulting synthetic images preserve generative artifacts while maintaining close alignment with real data, both spectrally and spatially—guiding the model to learn meaningful rather than spurious features.

The generalizability of DDA is built upon two foundations: 1) **VAE artifacts generalize across generators**. Because VAE-reconstructed images are the closest synthetic counterparts to real images, decision boundaries learned from these pairs are likely to remain effective for distinguishing other, more distant synthetic variants (e.g., those from text-to-image generators). Moreover, since the VAE decoder is typically the final stage in diffusion-based generators, its artifacts are less influenced by subsequent modules. 2) **Dual-domain alignment mitigates dataset bias**. By aligning synthetic images with real ones in both the frequency and pixel domains, DDA reduces real-synthetic discrepancies more effectively than alternative reconstruction-based methods. In particular, it eliminates high-frequency bias—commonly introduced by compression or generative artifacts—leading to stronger generalization and reduced reliance on spurious features.

**Comparison to Dataset Alignment Methods.** We validate that DDA creates the closest real-synthetic image pairs when compared to other alignment methods from the following three viewpoints: 1) Pixel domain: Left of Figure 7 shows that DDA-aligned images lead to minimal MSE loss compared to the original image; 2) Frequency domain: Right of Figure 7 shows that DDA-aligned images are most similar to the original image in frequency space; 3) Feature domain: Figure 8 validates that the cluster center of DDA-aligned images is closest to the center of real images.

## 4 Experiments

### 4.1 Experimental Setup

**Datasets** All compared detectors are evaluated on eight diverse datasets, including four benchmark datasets (GenImage [42], DRCT-2M [4], EvalGEN, and Synthbuster [1]) and three in-the-wild datasets (Chameleon [36], WildRF [2], and SynthWildx [6]), where images are sourced from the web. These datasets contain real images from different sources and various generators, including diffusion

Table 2: Datasets Overview. "SD" is stable diffusion and "AR" is auto-regressive model.

Dataset	Real / Fake	Source	# Models	Model Types
DDA-COCO	5K / 30K	MSCOCO	6	SD
GenImage [42]	48K / 48K	ImageNet	8	SD & GAN
DRCT-2M [4]	5K / 80K	MSCOCO	16	SD
Synthbuster [1]	1K / 9K	RAISE	9	SD & AR
EvalGEN	0 / 55.3K	Prompt	7	SD & AR
Chameleon [36]	14.9K / 11.2K	Internet	unknown	unknown
WildRF [2]	500 / 500	Reddit, FB, X	unknown	unknown
SynthWildx [6]	500 / 1.5K	X	5	SD & AR

Table 3: Comparison on DDA-COCO.

Method	real	fake					
		XL	EMA	MSE	SD21	SD35	Avg.
NPR <sub>(DCCV24)</sub> [7]	55.4	21.0	31.0	29.8	29.1	29.6	28.1 ± 4.0
UnivFD <sub>(CVPR23)</sub> [26]	99.2	2.7	5.3	3.8	4.3	1.9	3.6 ± 1.3
FatFormer <sub>(CVPR24)</sub> [25]	96.4	2.3	3.1	4.2	4.3	2.4	3.3 ± 0.9
SAFE <sub>(IJCV23)</sub> [21]	98.8	0.5	0.6	0.5	0.4	0.3	0.5 ± 0.1
C2P-CLIP <sub>(AAAI23)</sub> [31]	99.5	1.6	1.7	2.2	2.2	2.3	2.0 ± 0.3
AIDE <sub>(ICLR23)</sub> [36]	98.8	1.1	2.2	0.9	0.8	1.0	1.2 ± 0.6
DRCT <sub>(ICM23)</sub> [4]	94.2	24.5	34.7	33.1	33.6	26.3	30.4 ± 4.7
AlignedForensics <sub>(ICLR23)</sub> [27]	99.8	82.5	99.2	99.0	99.0	33.2	86.6 ± 20.0
VAE Rec.	94.4	94.3	96.2	96.3	96.6	66.4	90.0 ± 12.2
VAE Rec. + DDA (ours)	96.8	98.3	99.7	99.9	99.8	73.9	94.3 ± 11.4

models, GAN models, auto-regressive models, and other unknown models. They differ in format, content, and resolution, thereby minimizing evaluation bias. Table 2 outlines the datasets’ details.

**DDA-COCO and EvalGEN** DDA-COCO consists of five subsets containing reconstructed images of MSCOCO [22] validation set by different VAEs, utilizing frequency-level alignment. We construct the EvalGEN dataset using the five latest text-to-image (T2I) generators using aligned prompts from the GenEval benchmark [10]. Notably, **we are the first work to involve auto-regressive-based T2I generators for image forensics** in the AIGI detection field. Specifically, we introduce each generator as follows: (1) **Flux** [20]: the SOTA diffusion-based generator, offering extremely higher-resolution output images. (2) **GoT** [9]: A multimodal model combining LLM and diffusion processes to enable reasoning-guided image generation. (3) **Infinity** [15]: A bitwise auto-regressive model using infinite-vocabulary tokenization and self-correction for faster and higher-fidelity image generation. (4) **OmiGen** [35]: A unified multimodal framework capable of handling diverse image generation tasks within a single, simplified architecture. (5) **NOVA** [8]: A non-quantized auto-regressive model designed for efficient image and video generation, achieving high fidelity with reduced computational overhead. These models allow our **EvalGEN to serve as a very high-quality benchmark** for evaluating the generalizability of detectors on unseen generators.

**Implementation Details** We utilize DINOv2 as the backbone and fine-tune it using LoRA with a rank of 8. The input size is set to 336×336, using random cropping during training and center cropping during validation. Padding is applied when the image height or width is insufficient. The training data exclusively consists of MSCOCO [23] images and their DDA-aligned counterparts. All evaluations of DDA are performed using a single model, without any dataset-specific fine-tuning. More implementation details are omitted into Appendix due to space constraint.

**Evaluation Metrics and Comparative Methods** Unless otherwise specified, we report balanced accuracy, defined as the average of real and fake class accuracies, following the mainstream line of works [7, 26, 25, 21, 31, 36, 4, 27, 13], to evaluate the effectiveness and generalizability of detection methods. The compared methods include four frequency-based detectors: NPR [7], SAFE [21] and AIDE [36], three CLIP-based detectors: UnivFD [26], Fatformer [25] and C2P-CLIP [31] and two data alignment methods: DRCT [4] and AlignedForensics [27]. For fairness and reproducibility, we use publicly released checkpoints from the official GitHub repositories of these methods.<sup>2</sup>

## 4.2 Cross-Dataset Comparison

**Comparison on DDA-COCO** Table 3 reports real and fake accuracy scores on our proposed DDA-COCO. We observe the following: (1) Our method, trained solely on SD 2.1 reconstructed data, generalizes well to other diffusion models—surpassing the second-best by 7.7% in fake accuracy—and exhibits a smaller standard deviation than second-best detector. This suggests the model has learned a universal upsampling artifact present across diverse generative models, supporting the claim that better data alignment improves generalizability. We hypothesize that this artifact arises during the VAE-based decoding process (2) Furthermore, the DDA-COCO results highlight the importance of data alignment. Methods lacking alignment—such as NPR [7], UnivFD [26], FatFormer [25], C2P-CLIP [31], AIDE [36], and SAFE [21]—show large disparities between real and fake accuracy, revealing biases related to format, content, or resolution, as discussed in [31, 41]. AlignedForensics [27], which applies partial alignment (format & content), achieves higher performance—86.6% fake accuracy—further confirming alignment’s effectiveness.

<sup>2</sup>B-Free [13] is excluded from comparison except WildRF due to the lack of publicly available code and insufficient experimental reporting from original paper, which makes faithful reproduction prohibitively expensive and unreliable. For WildRF, we use the reported results from the original paper.

Table 4: Performance comparison on the DRCT-2M benchmark. “VAE Rec.” denotes training with SD21 VAE-reconstructed images using the same architecture and training settings as our method, but without Dual Data Alignment (DDA). “VAE Rec. + DDA (ours)” represents our full approach, applying DDA on top of the VAE-reconstructed training set. Bold numbers indicate the best performance per column; underlined numbers indicate the second-best.

Method	LDM	SDv1.4	SDv1.5	SDv2	SDXL	SDXL-Refiner	SD-Turbo	SDXL-Turbo	LDM-SDv1.5	LDM-SDXL	SDv1-Ctrl	SDv2-Ctrl	SDXL-Ctrl	SDv1-DR	SDv2-DR	SDXL-DR	Avg.
NPR <a href="#">(CCV24)</a> [7]	33.0	29.1	29.0	35.1	33.2	28.4	27.9	29.4	30.2	28.4	28.3	34.7	67.9	67.4	66.1	37.3 ± 15.0	
UnivFD <a href="#">(CVPR23)</a> [26]	85.4	56.8	56.4	58.2	63.2	55.0	56.5	53.0	54.5	65.9	68.0	65.4	75.9	64.6	56.2	53.9	61.8 ± 8.9
FatFormer <a href="#">(CVPR24)</a> [25]	55.9	48.2	48.2	48.2	48.2	48.2	48.3	48.2	48.3	50.6	49.7	49.9	59.8	66.3	60.6	56.0	52.2 ± 5.7
SAFE <a href="#">(KDDP25)</a> [21]	50.3	50.1	50.0	50.0	49.9	50.1	50.0	50.0	50.1	50.0	49.9	50.0	54.7	98.2	98.5	97.3	59.3 ± 19.2
C2P-CLIP <a href="#">(AAAI25)</a> [31]	83.0	51.7	51.7	52.9	51.9	64.6	51.7	50.6	52.0	66.1	56.9	54.7	77.8	67.2	57.1	56.7	59.2 ± 9.9
AIDE <a href="#">(ICLR25)</a> [36]	64.4	74.9	75.1	58.5	53.5	66.3	52.8	70.0	54.3	65.9	53.6	53.9	95.3	73.3	69.0	64.6 ± 11.8	
DRCT <a href="#">(ICML24)</a> [4]	96.7	96.3	96.3	94.9	96.2	93.5	93.4	92.9	91.2	95.0	95.6	92.7	92.0	94.1	69.6	57.4	90.5 ± 7.4
AlignedForensics <a href="#">(ICLR25)</a> [27]	<b>99.9</b>	<b>99.9</b>	<b>99.9</b>	<b>99.6</b>	90.2	81.3	<b>99.7</b>	89.4	<b>99.7</b>	90.0	<b>99.9</b>	<b>99.2</b>	87.6	<b>99.9</b>	<b>99.8</b>	92.6	95.5 ± 6.1
VAE Rec.	97.5	96.5	95.8	96.4	95.2	94.1	93.4	91.9	93.9	96.8	96.9	97.1	97.4	97.3	97.5	95.5	95.8 ± 1.7
VAE Rec. + DDA (ours)	98.4	98.1	97.8	97.5	<b>96.2</b>	<b>96.3</b>	96.6	<b>95.4</b>	97.5	<b>97.9</b>	98.2	98.2	<b>98.4</b>	98.1	98.4	<b>96.2</b>	<b>97.4</b> ± 1.2

Table 5: Comparison on GenImage.

Method	Midjourney	SDv1.4	SDv1.5	ADM	GLIDE	Wukong	VQDM	BigGAN	Avg.
NPR <a href="#">(CCV24)</a> [7]	53.4	55.1	55.0	43.8	41.2	57.4	48.4	57.7	51.5 ± 6.3
UnivFD <a href="#">(CVPR23)</a> [26]	55.1	55.6	55.7	62.5	61.3	61.1	76.9	84.4	64.1 ± 10.8
FatFormer <a href="#">(CVPR24)</a> [25]	52.1	53.6	53.8	61.4	65.5	60.9	72.5	82.2	62.8 ± 10.4
SAFE <a href="#">(KDDP25)</a> [21]	49.0	49.7	49.8	49.5	53.0	50.3	50.2	50.9	50.3 ± 1.2
C2P-CLIP <a href="#">(AAAI25)</a> [31]	86.6	77.5	76.9	71.6	73.5	79.4	73.7	85.9	74.4 ± 8.4
AIDE <a href="#">(ICLR25)</a> [36]	58.2	77.2	77.4	50.4	54.6	70.5	50.8	50.6	61.2 ± 11.9
DRCT <a href="#">(ICML24)</a> [4]	82.4	88.3	88.2	76.9	86.1	87.9	85.8	84.7 ± 2.7	
AlignedForensics <a href="#">(ICLR25)</a> [27]	<b>97.5</b>	<b>99.7</b>	<b>99.6</b>	52.4	57.6	<b>99.6</b>	75.0	80.6	79.0 ± 22.7
VAE Rec.	87.1	91.0	89.7	82.7	74.7	90.7	84.2	89.4	86.2 ± 5.2
VAE Rec. + DDA (ours)	94.4	92.3	92.2	<b>94.3</b>	<b>93.1</b>	92.3	<b>94.6</b>	<b>95.8</b>	<b>95.5</b> ± 1.6

Table 6: Comparison on EvalGEN.

Method	Flux	GoT	Infinity	OmniGen	NOVA	Avg.
NPR <a href="#">(CCV24)</a> [7]	52.0	41.6	77.2	64.2	61.2	59.2 ± 2.0
UnivFD <a href="#">(CVPR23)</a> [26]	4.0	9.2	15.7	8.3	39.6	15.4 ± 0.7
FatFormer <a href="#">(CVPR24)</a> [25]	9.9	47.8	44.7	98.3	27.3	45.6 ± 33.1
SAFE <a href="#">(KDDP25)</a> [21]	1.0	0.5	1.9	0.6	1.6	1.1 ± 0.1
C2P-CLIP <a href="#">(AAAI25)</a> [31]	8.7	49.4	35.1	86.4	18.8	38.9 ± 31.1
AIDE <a href="#">(ICLR25)</a> [36]	16.2	21.6	4.0	14.9	18.4	15.0 ± 6.7
DRCT <a href="#">(ICML24)</a> [4]	72.2	81.4	77.8	84.8	72.5	77.7 ± 5.5
AlignedForensics <a href="#">(ICLR25)</a> [27]	45.0	84.4	79.6	90.8	85.2	77.0 ± 18.3
VAE Rec.	64.0	89.6	88.2	88.6	89.7	84.2 ± 11.3
VAE Rec. + DDA (ours)	<b>87.0</b>	<b>99.3</b>	<b>99.5</b>	<b>99.5</b>	<b>100.0</b>	<b>94.0</b> ± 5.6

Table 7: Comparison on Synthbuster.

Method	DALL-E 2	DALL-E 3	Firefly	GLIDE	Midjourney	SD 1.3	SD 1.4	SD 2	SDXL	Avg.
NPR <a href="#">(CCV24)</a> [7]	51.1	49.3	46.5	48.5	52.8	51.4	51.8	46.0	52.8	50.0 ± 2.6
UnivFD <a href="#">(CVPR23)</a> [26]	83.5	47.4	89.9	53.3	52.5	70.4	69.9	75.7	68.0	67.8 ± 14.4
FatFormer <a href="#">(CVPR24)</a> [25]	59.4	39.5	60.3	72.7	44.4	53.7	54.0	52.3	69.1	56.1 ± 10.7
SAFE <a href="#">(KDDP25)</a> [21]	58.0	9.9	10.3	52.2	56.7	59.4	59.1	53.0	59.5	46.5 ± 20.8
C2P-CLIP <a href="#">(AAAI25)</a> [31]	55.6	63.2	59.5	86.7	52.9	75.2	76.7	69.2	77.7	68.5 ± 11.4
AIDE <a href="#">(ICLR25)</a> [36]	34.9	33.7	24.8	65.0	57.5	74.1	73.7	53.2	68.4	53.9 ± 18.6
DRCT <a href="#">(ICML24)</a> [4]	77.2	86.6	84.1	82.6	73.7	86.6	86.6	83.2	71.3	84.8 ± 3.6
AlignedForensics <a href="#">(ICLR25)</a> [27]	50.2	48.9	51.7	53.5	<b>98.7</b>	<b>98.8</b>	<b>98.8</b>	<b>98.6</b>	<b>97.3</b>	77.4 ± 25.0
VAE Rec.	86.0	86.1	85.8	78.1	86.1	86.0	86.1	86.0	86.3	85.2 ± 2.7
VAE Rec. + DDA (ours)	<b>95.3</b>	<b>95.2</b>	<b>95.4</b>	<b>88.9</b>	95.5	95.4	95.5	95.4	95.5	<b>94.6</b> ± 2.2

Table 8: Comparison on Chameleon, SynthWildX.

Method	Chameleon	SynthWildX			
		DALL-E 3	Firefly	Midjourney	Avg.
NPR <a href="#">(CCV24)</a> [7]	59.9	43.6	61.3	44.5	49.8 ± 10.0
UnivFD <a href="#">(CVPR23)</a> [26]	50.7	45.4	65.3	46.2	52.3 ± 11.3
FatFormer <a href="#">(CVPR24)</a> [25]	51.2	46.5	61.6	48.3	52.1 ± 8.2
SAFE <a href="#">(KDDP25)</a> [21]	59.2	49.4	48.2	49.6	49.1 ± 0.7
C2P-CLIP <a href="#">(AAAI25)</a> [31]	51.1	56.9	61.4	53.0	57.1 ± 4.2
AIDE <a href="#">(ICLR25)</a> [36]	63.1	63.4	48.8	51.9	48.8 ± 0.8
DRCT <a href="#">(ICML24)</a> [4]	56.6	58.3	56.4	50.5	55.1 ± 1.8
AlignedForensics <a href="#">(ICLR25)</a> [27]	71.0	85.5	58.5	92.2	78.8 ± 17.8
VAE Rec.	62.8	82.4	81.7	81.4	77.1 ± 9.5
VAE Rec. + DDA (ours)	74.3	<b>88.0</b>	<b>86.3</b>	<b>87.5</b>	<b>84.0</b> ± 6.5

Table 9: Comparison on WildRF.

Method	Facebook	Reddit	Twitter	Avg.
NPR <a href="#">(CCV24)</a> [7]	78.1	61.0	51.3	63.5 ± 13.6
UnivFD <a href="#">(CVPR23)</a> [26]	49.1	60.2	56.5	55.3 ± 5.7
FatFormer <a href="#">(CVPR24)</a> [25]	54.1	68.1	54.4	58.9 ± 8.0
SAFE <a href="#">(KDDP25)</a> [21]	50.9	74.1	37.5	57.2 ± 18.5
C2P-CLIP <a href="#">(AAAI25)</a> [31]	54.4	68.4	55.9	59.6 ± 7.7
AIDE <a href="#">(ICLR25)</a> [36]	57.8	71.5	45.8	58.4 ± 12.9
DRCT <a href="#">(ICML24)</a> [4]	46.6	53.1	55.2	50.6 ± 3.5
AlignedForensics <a href="#">(ICLR25)</a> [27]	89.4	69.1	81.8	80.1 ± 10.3
B-Free <a href="#">(CVPR24)</a> [13]	<b>95.6</b>	86.2	<b>97.3</b>	93.3 ± 9.4
VAE Rec.	89.5	91.8	93.5	88.3 ± 2.1
VAE Rec. + DDA (ours)	94.4	<b>94.3</b>	<b>96.8</b>	<b>95.1</b> ± 6.4

**Comparison on DRCT-2M, GenImage and Synthbuster** Tables 4, 5, and 7 summarize comparisons on DRCT-2M, GenImage, and Synthbuster, respectively. We observe the following: (1) Our method outperforms the second-best approach by 1.9%, 10.8%, and 9.8% on the three datasets. Given the diversity of real image sources and the inclusion of both GAN- and diffusion-based models, these results strongly support the effectiveness and generalizability of our method. (2) Consistent with observations on DDA-COCO, detectors trained with better-aligned data consistently achieve higher accuracy. This reinforces the importance of proper alignment. Notably, DDA consistently outperforms the VAE Rec. baseline by a non-trivial margin across all benchmarks, underscoring the critical contribution of dual-domain alignment in enhancing detection robustness.

**Comparison on EvalGEN** Table 6 presents the balanced accuracy on the EvalGEN dataset. Our method surpasses the second-best approach by 14.8%, demonstrating strong generalizability. This superior performance on new generators supports the effectiveness and robustness of our detector. Among the models in EvalGEN, FLUX poses the greatest challenge due to the high realism of its generated images. While our method performs relatively lower on FLUX compared to other models, it still significantly outperforms the second-best approach by 8.6%.

**Comparison on In-the-wild Datasets** Tables 8 and 9 demonstrate the balanced accuracy across three in-the-wild datasets. Our WildRF evaluation adopts the inference settings of B-Free [13]. We observe that: (1) Our method outperforms the second-best performing approach by 3.3%, 5.2% and 1.8% on Chameleon, SynthWildX and WildRF, while maintaining a relatively low standard deviation, indicating effectiveness and robustness in real-world scenarios. (2) To investigate the notably poor performance across detectors on the Chameleon dataset, we analyze its real images and identify widespread post-processing artifacts. These artifacts likely impeded the detection of synthetic patterns.

Table 10: Comparing on data generation time.

Method	# Real / Fake	Generation Method	Time Per Image	Full Construction Time
DRCT	11.8K / 35.4K	Diff. Rec.	0.6569 ± 0.0050 s	6.46 h
AlignedForensics	179K / 179K	VAE Rec.	0.1756 ± 0.0692 s	8.73 h
B-Free	51K / 309K	Diff. Rec + Inpaint.	3.0150 ± 0.0125 s	258.79 h
<b>VAE Rec. + DDA (ours)</b>	<b>11.8K / 11.8K</b>	<b>VAE Rec. + DDA</b>	<b>0.1792 ± 0.0704 s</b>	<b>0.59 h</b>

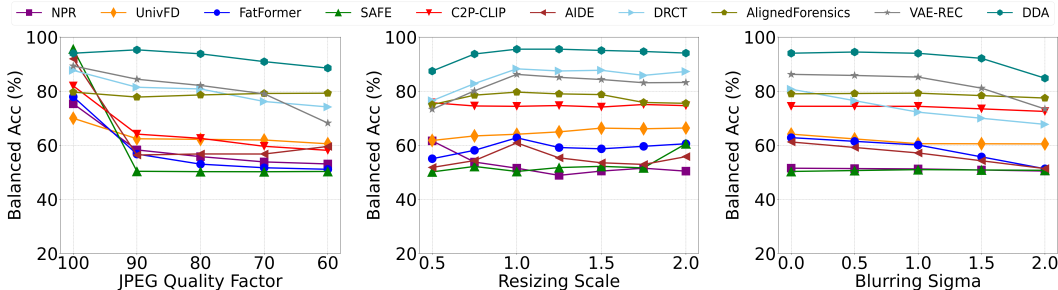
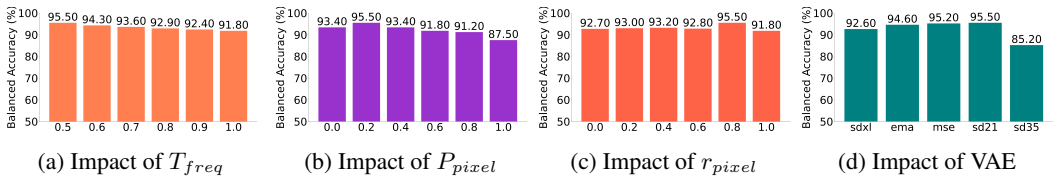


Figure 9: Robustness analysis on GenImage.



(a) Impact of  $T_{freq}$  (b) Impact of  $P_{pixel}$  (c) Impact of  $R_{pixel}$  (d) Impact of VAE  
 Figure 10: **Ablation studies.** (a)  $T_{freq}$ : frequency threshold for frequency-level alignment; (b)  $P_{pixel}$ : probability of applying pixel-level alignment; (c)  $R_{pixel}$ : upper bound for sampling the pixel mixup ratio; (d) VAE: backbone used for training data reconstruction. Results show the impact of each hyperparameter on the performance of DDA.

**Comparison on Generation Time Cost** We compare three methods which introduce train data generation—DRCT [4], AlignedForensics [27], and B-Free [13]. Table 10 presents the number of real and fake images used for training, generation method and the estimated reconstruction time (Single Image & Full Set) using each method, which is tested by generating 100 synthetic images. Results show that our DDA requires the least amount of training data and reconstruction time, confirming its effectiveness and efficiency in terms of training cost.

### 4.3 Evaluation on Robustness

Figure 9 shows the results of three robustness evaluations on the GenImage-JPEG96 dataset for all compared methods. Results show that: (1) DDA shows strong robustness across all three post-processing methods, outperforming the second-best method by 9.3%, 6.8%, and 7.3% under JPEG 60, RESIZE 2.0, and BLUR 2.0, respectively. (2) Methods lacking alignment, such as NPR [7], SAFE [21], and AIDE [36], demonstrate poor robustness under JPEG compression and resizing. In contrast, methods with alignment like DRCT [4] and AlignedForensics [27] perform better, emphasizing the importance of data alignment. (3) All detectors are less robust to downsampling than upsampling, which we argue that the former irreversibly discards image details while the latter preserves the original content.

### 4.4 Ablation Studies

Figure 10 illustrates the impact of  $T_{freq}$ ,  $P_{pixel}$ ,  $R_{pixel}$ , and the choice of VAE in training data generation. Results indicate that a  $T_{freq}$  value of 0.5 yields the best performance. The detector maintains consistent accuracy when  $P_{pixel}$  and  $R_{pixel}$  are between 0.2 and 0.8, with performance drops observed at 0.0 and 1.0, confirming the effectiveness of pixel-level alignment. Experiments with different VAEs confirm that SD21 is the most effective choice for training data generation.

## 5 Conclusion

In this paper, we first reveal that single reconstruction is insufficient for fully aligning real and synthetic image pairs. Building on this insight, we propose DDA to align synthetic images with real ones across pixel and frequency domains, thereby mitigating bias in AIGI detectors. We also introduce two AIGI datasets. DDA-COCO and EvalGEN. Extensive experiments on eight datasets

demonstrate that our method outperforms state-of-the-art baselines by a margin of 7.5% on in-the-wild benchmark. We believe that DDA, DDA-COCO, and EvalGEN form a solid foundation for advancing the effectiveness and generalization of the whole AIGI detection field.

**Limitations and Future Work** While our method shows strong performance on both benchmarks and real-world data, it remains sensitive to heavily post-processed images, as seen in the Chameleon dataset. Interestingly, we also observed that even photos taken by smartphones may exhibit synthetic-like artifacts—likely due to the AI-based enhancement features embedded in modern smartphone camera pipelines. In future work, we plan to: (1) clarify the boundary between real and synthetic images in post-processed content, and (2) extend DDA to video-based detection tasks to support generalization in AI-generated video detection.

## References

- [1] Quentin Bammey. Synthbuster: Towards detection of diffusion model generated images. *IEEE Open Journal of Signal Processing*, 5:1–9, 2023.
- [2] Bar Cavia, Eliahu Horwitz, Tal Reiss, and Yedid Hoshen. Real-time deepfake detection in the real-world. *arXiv preprint arXiv:2406.09398*, 2024.
- [3] George Cazenavette, Avneesh Sud, Thomas Leung, and Ben Usman. Fakeinversion: Learning to detect images from unseen text-to-image models by inverting stable diffusion. In *Proceedings of the IEEE/CVF Conference on Computer Vision and Pattern Recognition*, pages 10759–10769, 2024.
- [4] Baoying Chen, Jishen Zeng, Jianquan Yang, and Rui Yang. Drct: Diffusion reconstruction contrastive training towards universal detection of diffusion generated images. In *Forty-first International Conference on Machine Learning*, 2024.
- [5] Beilin Chu, Xuan Xu, Xin Wang, Yufei Zhang, Weike You, and Linna Zhou. Fire: Robust detection of diffusion-generated images via frequency-guided reconstruction error. In *CVPR*, 2025.
- [6] Davide Cozzolino, Giovanni Poggi, Riccardo Corvi, Matthias Nießner, and Luisa Verdoliva. Raising the bar of ai-generated image detection with clip. In *Proceedings of the IEEE/CVF Conference on Computer Vision and Pattern Recognition*, pages 4356–4366, 2024.
- [7] Davide Cozzolino, Giovanni Poggi, Matthias Nießner, and Luisa Verdoliva. Zero-shot detection of ai-generated images. In *European Conference on Computer Vision*, pages 54–72. Springer, 2024.
- [8] Haoge Deng, Ting Pan, Haiwen Diao, Zhengxiong Luo, Yufeng Cui, Huchuan Lu, Shiguang Shan, Yonggang Qi, and Xinlong Wang. Autoregressive video generation without vector quantization. *arXiv preprint arXiv:2412.14169*, 2024.
- [9] Rongyao Fang, Chengqi Duan, Kun Wang, Linjiang Huang, Hao Li, Shilin Yan, Hao Tian, Xingyu Zeng, Rui Zhao, Jifeng Dai, et al. Got: Unleashing reasoning capability of multimodal large language model for visual generation and editing. *arXiv preprint arXiv:2503.10639*, 2025.
- [10] Dhruva Ghosh, Hannaneh Hajishirzi, and Ludwig Schmidt. Geneval: An object-focused framework for evaluating text-to-image alignment. *Advances in Neural Information Processing Systems*, 36:52132–52152, 2023.
- [11] Ian J Goodfellow et al. Generative adversarial nets. In *Advances in Neural Information Processing Systems*, 2014.
- [12] Patrick Grommelt, Louis Weiss, Franz-Josef Pfreundt, and Janis Keuper. Fake or jpeg? revealing common biases in generated image detection datasets. *arXiv preprint arXiv:2403.17608*, 2024.
- [13] Fabrizio Guillaro, Giada Zingarini, Ben Usman, Avneesh Sud, Davide Cozzolino, and Luisa Verdoliva. A bias-free training paradigm for more general ai-generated image detection. *arXiv preprint arXiv:2412.17671*, 2024.

- [14] Seoyeon Gye, Junwon Ko, Hyounguk Shon, Minchan Kwon, and Junmo Kim. Sfld: Reducing the content bias for ai-generated image detection. *arXiv preprint arXiv:2502.17105*, 2025.
- [15] Jian Han, Jinlai Liu, Yi Jiang, Bin Yan, Yuqi Zhang, Zehuan Yuan, Bingyue Peng, and Xiaobing Liu. Infinity: Scaling bitwise autoregressive modeling for high-resolution image synthesis. *arXiv preprint arXiv:2412.04431*, 2024.
- [16] Jonathan Ho et al. Denoising diffusion probabilistic models. *Advances in Neural Information Processing Systems*, 33:6840–6851, 2020.
- [17] Dimitrios Karageorgiou, Symeon Papadopoulos, Ioannis Kompatsiaris, and Efstratios Gavves. Any-resolution ai-generated image detection by spectral learning. In *CVPR*, 2025.
- [18] Tero Karras et al. Progressive growing of gans for improved quality, stability, and variation. In *International Conference on Learning Representations*, 2018.
- [19] Tero Karras et al. A style-based generator architecture for generative adversarial networks. In *Proceedings of the IEEE/CVF Conference on Computer Vision and Pattern Recognition*, pages 4401–4410, 2019.
- [20] Black Forest Labs. Flux. <https://github.com/black-forest-labs/flux>, 2024.
- [21] Ouxiang Li, Jiayin Cai, Yanbin Hao, Xiaolong Jiang, Yao Hu, and Fuli Feng. Improving synthetic image detection towards generalization: An image transformation perspective. *arXiv preprint arXiv:2408.06741*, 2024.
- [22] Tsung-Yi Lin et al. Microsoft coco: Common objects in context. In *European Conference on Computer Vision*, pages 740–755. Springer, 2014.
- [23] Tsung-Yi Lin, Michael Maire, Serge Belongie, James Hays, Pietro Perona, Deva Ramanan, Piotr Dollár, and C Lawrence Zitnick. Microsoft coco: Common objects in context. In *Computer vision—ECCV 2014: 13th European conference, zurich, Switzerland, September 6-12, 2014, proceedings, part v 13*, pages 740–755. Springer, 2014.
- [24] Honggu Liu et al. Spatial-phase shallow learning: rethinking face forgery detection in frequency domain. In *Proceedings of the IEEE/CVF Conference on Computer Vision and Pattern Recognition*, pages 772–781, 2021.
- [25] Huan Liu, Zichang Tan, Chuangchuang Tan, Yunchao Wei, Jingdong Wang, and Yao Zhao. Forgery-aware adaptive transformer for generalizable synthetic image detection. In *Proceedings of the IEEE/CVF Conference on Computer Vision and Pattern Recognition*, pages 10770–10780, 2024.
- [26] Utkarsh Ojha et al. Towards universal fake image detectors that generalize across generative models. In *Proceedings of the IEEE/CVF Conference on Computer Vision and Pattern Recognition*, pages 24480–24489, 2023.
- [27] Anirudh Sundara Rajan, Utkarsh Ojha, Jedidiah Schloesser, and Yong Jae Lee. Aligned datasets improve detection of latent diffusion-generated images, 2025.
- [28] Robin Rombach et al. High-resolution image synthesis with latent diffusion models. In *Proceedings of the IEEE/CVF Conference on Computer Vision and Pattern Recognition*, pages 10684–10695, 2022.
- [29] Zeyang Sha, Zheng Li, Ning Yu, and Yang Zhang. De-fake: Detection and attribution of fake images generated by text-to-image generation models. In *Proceedings of the 2023 ACM SIGSAC conference on computer and communications security*, pages 3418–3432, 2023.
- [30] Chuangchuang Tan et al. Learning on gradients: Generalized artifacts representation for gan-generated images detection. In *Proceedings of the IEEE/CVF Conference on Computer Vision and Pattern Recognition (CVPR)*, pages 12105–12114, June 2023.
- [31] Chuangchuang Tan, Renshuai Tao, Huan Liu, Guanghua Gu, Baoyuan Wu, Yao Zhao, and Yunchao Wei. C2p-clip: Injecting category common prompt in clip to enhance generalization in deepfake detection. In *Proceedings of the AAAI Conference on Artificial Intelligence*, 2024.

- [32] Chuangchuang Tan, Yao Zhao, Shikui Wei, Guanghua Gu, Ping Liu, and Yunchao Wei. Frequency-aware deepfake detection: Improving generalizability through frequency space domain learning. In *Proceedings of the AAAI Conference on Artificial Intelligence*, volume 38, pages 5052–5060, 2024.
- [33] Chuangchuang Tan, Yao Zhao, Shikui Wei, Guanghua Gu, Ping Liu, and Yunchao Wei. Rethinking the up-sampling operations in cnn-based generative network for generalizable deepfake detection. In *Proceedings of the IEEE/CVF Conference on Computer Vision and Pattern Recognition*, pages 28130–28139, 2024.
- [34] Sheng-Yu Wang et al. Cnn-generated images are surprisingly easy to spot... for now. In *Proceedings of the IEEE/CVF Conference on Computer Vision and Pattern Recognition*, pages 8695–8704, 2020.
- [35] Shitao Xiao, Yueze Wang, Junjie Zhou, Huaying Yuan, Xingrun Xing, Ruiran Yan, Chaofan Li, Shuting Wang, Tiejun Huang, and Zheng Liu. Omnigen: Unified image generation. *arXiv preprint arXiv:2409.11340*, 2024.
- [36] Shilin Yan, Ouxiang Li, Jiayin Cai, Yanbin Hao, Xiaolong Jiang, Yao Hu, and Weidi Xie. A sanity check for ai-generated image detection. *arXiv preprint arXiv:2406.19435*, 2024.
- [37] Zhiyuan Yan, Taiping Yao, Shen Chen, Yandan Zhao, Xinghe Fu, Junwei Zhu, Donghao Luo, Chengjie Wang, Shouhong Ding, Yunsheng Wu, et al. Df40: Toward next-generation deepfake detection. *arXiv preprint arXiv:2406.13495*, 2024.
- [38] Zhiyuan Yan, Junyan Ye, Weijia Li, Zilong Huang, Shenghai Yuan, Xiangyang He, Kaiqing Lin, Jun He, Conghui He, and Li Yuan. Gpt-imgeval: A comprehensive benchmark for diagnosing gpt4o in image generation. *arXiv preprint arXiv:2504.02782*, 2025.
- [39] Xiao Yu, Kejiang Chen, Kai Zeng, Han Fang, Zijin Yang, Xiuwei Shang, Yuang Qi, Weiming Zhang, and Nenghai Yu. Semgir: Semantic-guided image regeneration based method for ai-generated image detection and attribution. In *Proceedings of the 32nd ACM International Conference on Multimedia*, pages 8480–8488, 2024.
- [40] Yabo Zhang, Yuxiang Wei, Dongsheng Jiang, Xiaopeng Zhang, Wangmeng Zuo, and Qi Tian. Controlvideo: Training-free controllable text-to-video generation. *arXiv preprint arXiv:2305.13077*, 2023.
- [41] Chende Zheng, Chenhao Lin, Zhengyu Zhao, Hang Wang, Xu Guo, Shuai Liu, and Chao Shen. Breaking semantic artifacts for generalized ai-generated image detection. *Advances in Neural Information Processing Systems*, 37:59570–59596, 2024.
- [42] Mingjian Zhu, Hanting Chen, Qiangyu Yan, Xudong Huang, Guanyu Lin, Wei Li, Zhijun Tu, Hailin Hu, Jie Hu, and Yunhe Wang. Genimage: A million-scale benchmark for detecting ai-generated image. *Advances in Neural Information Processing Systems*, 36:77771–77782, 2023.

# Appendix

Appendix provides additional technical and evaluative details of our work. Section A presents **the implementation details** of our method. Section B summarizes **the peer methods**. Section C reports **More Comparison Results**, further evaluating effectiveness of our method. Section D presents **ablation studies on VAE, input size and backbone**. **More details of our proposed dataset EvalGEN** in Section E, providing some prompts used for generation and visualizing some images from EvalGEN. Finally, Section F **visualizes the regional detection results of DDA**.

## A Implementation Details

**Training Details** Our experiments were conducted on eight NVIDIA V100 GPUs. We train the detector using a dataset comprising MSCOCO images and their synthetic counterparts generated via DDA alignment using the VAE from Stable Diffusion 2.1. The model was trained with a base batch size of 16 and a learning rate of  $1e-4$ . To achieve an effective batch size of 512 without exceeding GPU memory limits, we applied gradient accumulation over 32 iterations. We evaluated balanced accuracy on all datasets every 2,500 iterations. To prevent overfitting, early stopping was employed: training was terminated if balanced accuracy failed to improve by at least 1%.

## B Peer Methods

Below we provide a brief description of the compared methods used in Section 4 of main paper.

**NPR [7]** This detector leverages low-level features—neighboring pixel relationships—to distinguish synthetic images from real ones. NPR trains a ResNet-50 to identify upsampling patterns.

**UnivFD [26]** Instead of conventional supervised training, this method utilizes features from a vision-language model (CLIP-ViT) combined with a linear classifier. This approach avoids overfitting to specific generative artifacts and generalizes better to unseen generators.

**FatFormer [25]** FatFormer builds on a ViT backbone, incorporating a forgery-aware adapter that adapts features in both the image and frequency domains. It introduces language-guided alignment using contrastive learning with text prompts to improve generalization.

**SAFE [21]** This method focuses on frequency domain artifacts. The detector is built upon a ResNet backbone and trained with several data augmentation techniques, including random masking.

**C2P-CLIP [31]** The method utilizes CLIP embeddings with category-specific prompts to enhance deepfake detection generalizability. Image captions are generated using ClipCap and enhanced with category common prompts. During training, these enhanced caption-image pairs train the image encoder through contrastive learning. For inference, only the modified image encoder and a linear classifier are used.

**AIDE [36]** This work employs a hybrid approach that combines low-level patch statistics with high-level semantics. It uses DCT scoring to select extreme frequency patches for extracting noise patterns through SRM filters, while utilizing CLIP embeddings to capture semantic information. These complementary features are fused through channel-wise concatenation before classification.

**DRCT [4]** This method reconstructs real images using diffusion models to generate challenging synthetic samples that retain visual content while introducing subtle artifacts. Contrastive learning is employed to guide detectors toward recognizing these fingerprints, improving generalization.

**AlignedForensics [27]** This method creates aligned datasets by reconstructing real images through a single forward pass in an LDM’s autoencoder. This forces the detector to focus exclusively on artifacts introduced by the VAE decoder, avoiding reliance on spurious correlations.

Table 11: **Overview of the comparison across all 10 datasets.** To ensure fairness and reproducibility, we use official checkpoints released by each method. We exclude B-Free [13] from this comparison due to the unavailability of public code. We add JPEG compression with quality factor 96 to GenImage, ForenSynth and AIGCDetectionBenchmark datasets to eliminate format bias. We also report the number of generators used in each dataset below each dataset name, where G refers to GANs, D to Diffusion models, and AR to Auto-Regressive models.

Method	Manually Curated Datasets							In-the-Wild Datasets			Avg	Min
	GenImage IG + 7D	DRCT-2M 16D	DDA-COCO 5D	EvalGEN 3D + 2AR	Synthbuster 9D	ForenSynth 11G	AIGCDetection Benchmark 7G + 9D	Chameleon Unknown	Synthwildx 3D	WildRF Unknown		
NPR [RCV24] [7]	51.5 ± 6.3	37.3 ± 15.0	28.1 ± 4.0	59.2 ± 2.0	50.0 ± 2.6	47.9 ± 22.6	53.1 ± 12.2	59.9	49.8 ± 10.0	63.5 ± 13.6	50.0 ± 10.7	28.1
UnivFD [CVPR24] [26]	64.1 ± 10.8	61.8 ± 8.9	3.6 ± 1.3	15.4 ± 0.7	67.8 ± 14.4	77.7 ± 16.1	72.5 ± 17.3	50.7	52.3 ± 11.3	55.3 ± 5.7	52.1 ± 24.2	3.6
FatFormer [CVPR24] [25]	62.8 ± 10.4	52.2 ± 5.7	3.3 ± 0.9	45.6 ± 33.1	56.1 ± 10.7	90.1 ± 11.8	85.0 ± 14.9	51.2	52.1 ± 8.2	58.9 ± 8.0	55.7 ± 23.6	3.3
SAFE [ICDIP24] [21]	50.3 ± 1.2	59.3 ± 19.2	0.5 ± 0.1	1.1 ± 0.1	46.5 ± 20.8	49.7 ± 2.7	50.3 ± 1.1	59.2	49.1 ± 0.7	57.2 ± 18.5	42.3 ± 22.3	0.5
C2P-CLIP [AAAI25] [31]	74.4 ± 8.4	59.2 ± 9.9	2.0 ± 0.3	38.9 ± 31.1	68.5 ± 11.4	92.1 ± 10.1	81.4 ± 15.6	51.1	57.1 ± 4.2	59.6 ± 7.7	58.4 ± 25.0	2.0
AIDE [ICLR25] [36]	61.2 ± 11.9	64.6 ± 11.8	1.2 ± 0.6	15.0 ± 6.7	53.9 ± 18.6	59.4 ± 24.6	63.6 ± 13.9	63.1	48.8 ± 0.8	58.4 ± 12.9	48.9 ± 22.3	1.2
DRCT [ICML24] [4]	84.7 ± 2.7	90.5 ± 7.4	30.4 ± 4.7	77.7 ± 5.5	84.8 ± 3.6	73.9 ± 13.4	81.4 ± 12.2	56.6	55.1 ± 1.8	50.6 ± 3.5	68.6 ± 19.4	30.4
AlignedForensics [ICLR25] [27]	79.0 ± 22.7	95.5 ± 6.1	86.6 ± 20.0	77.0 ± 18.3	77.4 ± 25.0	53.9 ± 7.1	66.6 ± 21.6	71.0	78.8 ± 17.8	80.1 ± 10.3	76.6 ± 11.2	53.9
<b>VAE Rec. + DDA (ours)</b>	<b>95.5 ± 1.6</b>	<b>97.4 ± 1.2</b>	<b>94.3 ± 11.4</b>	<b>94.0 ± 5.6</b>	<b>94.6 ± 2.2</b>	<b>85.5 ± 8.9</b>	<b>93.3 ± 5.4</b>	<b>74.3</b>	<b>84.0 ± 6.5</b>	<b>95.1 ± 1.4</b>	<b>90.8 ± 7.3</b>	<b>74.3</b>

Table 12: Comparison on AIGCDetectionBenchmark.

Method	ADM	DALLE2	GLIDE	Midjourney	VQDM	BigGAN	CycleGAN	GauGAN	ProGAN	SDXL	SD14	SD15	StarGAN	StyleGAN	StyleGAN2	WFR	Wukong	Avg.
NPR [RCV24] [7]	43.8	20.0	41.2	53.4	48.4	53.1	76.6	42.2	58.7	59.6	55.1	55.0	67.4	57.9	54.6	58.4	57.4	53.1 ± 12.2
UnivFD [CVPR24] [26]	60.5	50.0	61.3	55.1	78.9	87.5	98.9	38.8	92.4	58.2	55.6	55.7	95.1	80.0	69.4	69.2	61.1	72.5 ± 17.3
FatFormer [CVPR24] [25]	80.2	68.5	91.1	54.4	88.0	99.2	99.5	99.1	98.3	71.7	67.5	67.2	99.4	98.0	98.8	88.1	75.6	85.0 ± 14.9
SAFE [ICDIP24] [21]	49.5	49.5	53.0	49.0	50.2	52.2	51.9	50.0	50.0	49.8	49.7	49.8	50.1	50.0	50.0	49.8	50.3	50.3 ± 1.1
C2P-CLIP [AAAI25] [31]	71.6	52.3	73.5	56.6	73.7	98.4	96.8	96.8	99.3	62.3	77.5	76.9	99.6	93.1	79.4	94.8	79.4	81.4 ± 15.6
AIDE [ICLR25] [36]	52.9	51.1	60.2	49.8	69.3	70.1	93.6	60.6	89.0	49.6	51.6	51.0	72.1	66.5	59.0	80.6	54.5	63.6 ± 13.9
DRCT [ICML24] [4]	78.9	88.2	89.2	85.5	88.6	81.4	91.0	93.8	71.1	88.3	91.4	91.0	53.0	62.7	63.8	73.9	90.8	81.4 ± 12.2
AlignedForensics [ICLR25] [27]	51.6	52.0	55.6	96.2	72.1	51.2	49.5	50.8	50.7	95.1	99.7	99.6	53.8	52.7	51.6	50.0	99.6	66.6 ± 21.6
<b>VAE Rec. + DDA (ours)</b>	<b>94.3</b>	<b>98.8</b>	<b>93.1</b>	<b>94.4</b>	<b>94.6</b>	<b>93.9</b>	<b>90.7</b>	<b>94.5</b>	<b>90.0</b>	<b>98.6</b>	<b>97.3</b>	<b>97.2</b>	<b>88.7</b>	<b>93.6</b>	<b>92.9</b>	<b>75.8</b>	<b>97.3</b>	<b>93.3 ± 5.4</b>

Table 13: Comparison on ForenSynth.

Method	BigGAN	CRN	CycleGAN	DeepFake	GauGAN	IMLE	ProGAN	SAN	SeeingDark	StarGAN	StyleGAN	StyleGAN2	WFR	Avg.
NPR [RCV24] [7]	53.1	0.4	76.6	35.7	42.2	5.3	58.7	48.4	63.6	67.4	57.9	54.6	58.8	47.9 ± 22.6
UnivFD [CVPR24] [26]	87.5	55.7	96.9	69.4	98.8	68.1	99.4	58.2	62.2	95.1	80.0	69.4	69.2	77.7 ± 16.1
FatFormer [CVPR24] [25]	99.3	72.1	99.5	93.0	99.3	72.1	98.4	70.8	81.9	99.4	98.1	98.9	88.3	90.1 ± 11.8
SAFE [ICDIP24] [21]	52.2	50.0	51.9	50.1	50.0	50.0	50.9	41.1	50.1	50.0	50.0	50.0	49.8	49.7 ± 2.7
C2P-CLIP [AAAI25] [31]	98.4	93.8	96.8	92.6	98.8	93.2	99.3	63.2	94.7	99.6	93.1	79.4	94.8	92.1 ± 10.1
AIDE [ICLR25] [36]	70.1	12.2	93.6	53.2	60.6	15.9	89.0	55.3	44.2	72.1	66.5	59.0	80.6	59.4 ± 24.6
DRCT [ICML24] [4]	81.4	78.4	91.0	51.5	93.8	82.6	71.1	84.9	72.2	53.0	62.7	63.8	73.9	73.9 ± 13.4
AlignedForensics [ICLR25] [27]	51.2	50.4	49.5	71.7	50.8	49.7	50.7	67.6	51.4	53.8	52.7	51.6	50.0	53.9 ± 7.1
<b>VAE Rec. + DDA (ours)</b>	<b>93.9</b>	<b>71.3</b>	<b>90.7</b>	<b>83.2</b>	<b>94.5</b>	<b>71.3</b>	<b>90.0</b>	<b>90.2</b>	<b>75.6</b>	<b>88.7</b>	<b>83.6</b>	<b>92.9</b>	<b>75.8</b>	<b>85.5 ± 0.9</b>

Table 14: Detailed comparison with B-Free. We evaluate performance on Synthbuster and WildRF—two open-source datasets originally used in the B-Free. To ensure a fair comparison, we follow B-Free’s evaluation protocol by employing the test-time adaptation (TTA) technique, which averages logit scores over multiple image crops to represent each full image. The reported results for B-Free are cited directly from B-Free [13].

Method	Synthbuster					WildRF				
	DALLE-E 2	DALLE-E 3	Firefly	SDXL	Midjourney	Avg.	Facebook	Reddit	Twitter	Avg.
NPR [RCV24] [7]	51.1	49.3	46.5	52.8	52.8	50.6 ± 2.7	78.1	61.0	51.3	63.5 ± 13.6
UnivFD [CVPR24] [26]	51.1	49.3	46.5	68.0	52.8	53.5 ± 8.4	49.1	60.2	56.5	55.3 ± 5.7
FatFormer [CVPR24] [25]	59.4	39.5	60.3	69.1	44.4	54.5 ± 12.2	54.1	68.1	54.4	58.9 ± 8.0
SAFE [ICDIP24] [21]	58.0	9.9	10.3	59.5	56.7	38.9 ± 26.3	50.9	74.1	37.5	57.2 ± 18.5
C2P-CLIP [AAAI25] [31]	55.6	63.2	59.5	77.7	52.9	61.8 ± 9.7	54.4	68.4	55.9	59.6 ± 7.7
AIDE [ICLR25] [36]	34.9	33.7	24.8	68.4	57.5	43.9 ± 18.3	57.8	71.5	45.8	58.4 ± 12.9
DRCT [ICML24] [4]	77.2	86.6	84.1	71.3	73.7	78.6 ± 6.6	46.6	53.1	55.2	50.6 ± 3.5
AlignedForensics [ICLR25] [27]	50.2	48.9	51.7	97.3	98.7	69.4 ± 26.2	89.4	69.1	81.8	80.1 ± 10.3
B-Free [CVPR24] [13]	95.6	98.2	98.7	98.2	99.8	98.1 ± 1.5	95.6	86.2	97.3	93.3 ± 9.4
<b>VAE Rec. + DDA (ours)</b>	<b>99.0</b>	<b>98.6</b>	<b>99.1</b>	<b>99.1</b>	<b>99.1</b>	<b>99.0 ± 0.2</b>	<b>94.4</b>	<b>94.3</b>	<b>96.8</b>	<b>95.1 ± 1.4</b>

Table 15: Ablation study across different VAE-reconstructed train data.

VAE	GenImage	DRCT-2M	DDA-COCO	EvalGEN	Synthbuster	Chameleon	SynthWildx	Avg.
SDXL	91.6	97.6	95.0	97.6	88.7	72.6	80.3	89.1 ± 9.4
FT-EMA	93.6	97.1	97.4	93.8	93.1	69.7	82.8	89.6 ± 10.0
FT-MSE	94.2	97.0	94.9	94.4	93.5	68.9	86.1	89.9 ± 9.9
SD35	84.2	81.7	91.9	92.8	80.7	57.8	67.9	79.6 ± 12.7
SDXL+SD21+FT-EMA	91.6	97.1	95.7	93.1	94.0	68.4	84.9	89.3 ± 10.0
SD21	95.5	97.4	94.3	94.0	94.6	74.3	84.0	90.6 ± 8.4

**B-Free [13]** B-Free introduces a training paradigm using self-conditioned diffusion-based reconstructions. It ensures semantic alignment between real and synthetic images so that differences arise solely from generation artifacts. The approach includes content augmentation via inpainting and fine-tunes a DINOv2+reg ViT using large crops to retain forensic signals.

## C More Comparison Results

**Comprehensive Comparison on 10 Diverse Datasets** Table 11 presents a comprehensive comparison across 10 datasets—7 manually curated and 3 in-the-wild—encompassing nearly all known open-source AIGI evaluation benchmarks. Eight of these datasets were introduced earlier in the main paper, while the remaining two—AIGCDetectionBenchmark and ForenSynth—are newly introduced

Table 16: Ablation study across different input sizes.

Input Size	GenImage	DRCT-2M	DDA-COCO	EvalGEN	Synthbuster	Chameleon	SynthWildx	Avg
224	94.9	96.7	<b>95.9</b>	<b>97.2</b>	88.9	71.9	80.3	89.4 ± 9.8
252	<u>95.3</u>	96.7	95.0	94.1	92.4	72.0	84.0	89.9 ± 8.9
280	<b>95.7</b>	96.2	95.6	95.4	91.9	70.1	84.6	89.9 ± 9.7
392	92.9	96.5	92.0	95.7	93.9	71.8	<u>89.6</u>	<u>90.3</u> ± 8.5
448	93.4	<u>97.2</u>	90.7	89.5	<b>95.8</b>	65.7	<b>89.9</b>	88.9 ± 10.6
504	93.0	93.0	92.7	<u>95.8</u>	93.3	<u>73.2</u>	86.2	89.6 ± 7.8
<b>336</b>	95.5	<b>97.4</b>	94.3	94.0	<u>94.6</u>	<b>74.3</b>	84.0	<b>90.6</b> ± 8.4

Table 17: Ablation study across different detector backbones. **Linear Probing** refers to training a linear classifier on frozen backbone features. **LoRA Finetune** denotes fine-tuning the backbone using the LoRA (rank=8) method.

Train Strategy	Backbone	GenImage	DRCT-2M	DDA-COCO	EvalGEN	Synthbuster	Chameleon	SynthWildx	Avg
Linear Probing	CLIP ViT-B/16	86.4	84.2	67.8	92.3	54.0	54.7	53.9	70.5 ± 16.9
	CLIP ViT-B/32	83.8	80.8	79.6	97.3	49.3	63.2	54.5	72.7 ± 17.4
	CLIP ViT-L/14	91.2	<u>91.2</u>	80.6	98.9	62.2	59.1	52.8	76.6 ± 18.4
	DINOv2 ViT-S/14	68.8	74.4	66.7	59.8	68.2	60.9	62.6	65.9 ± 5.2
	DINOv2 ViT-B/14	68.3	74.5	66.3	66.2	69.8	64.1	58.6	66.8 ± 4.9
	DINOv2 ViT-L/14	70.5	75.6	65.8	56.8	<u>71.2</u>	60.6	61.6	66.0 ± 6.7
LoRA Finetune	CLIP ViT-B/16	95.2	80.3	<u>97.9</u>	96.2	55.5	46.6	62.0	76.2 ± 21.4
	CLIP ViT-B/32	93.2	80.6	95.6	<u>98.5</u>	49.6	55.0	59.0	75.9 ± 20.9
	CLIP ViT-L/14	<b>97.0</b>	80.4	<b>98.8</b>	<b>99.2</b>	68.3	<u>67.7</u>	<u>71.8</u>	<u>83.3</u> ± 14.7
	<b>DINOv2 ViT-L/14</b>	<u>95.5</u>	<b>97.4</b>	94.3	94.0	<b>94.6</b>	<b>74.3</b>	<b>84.0</b>	<b>90.6</b> ± 8.4

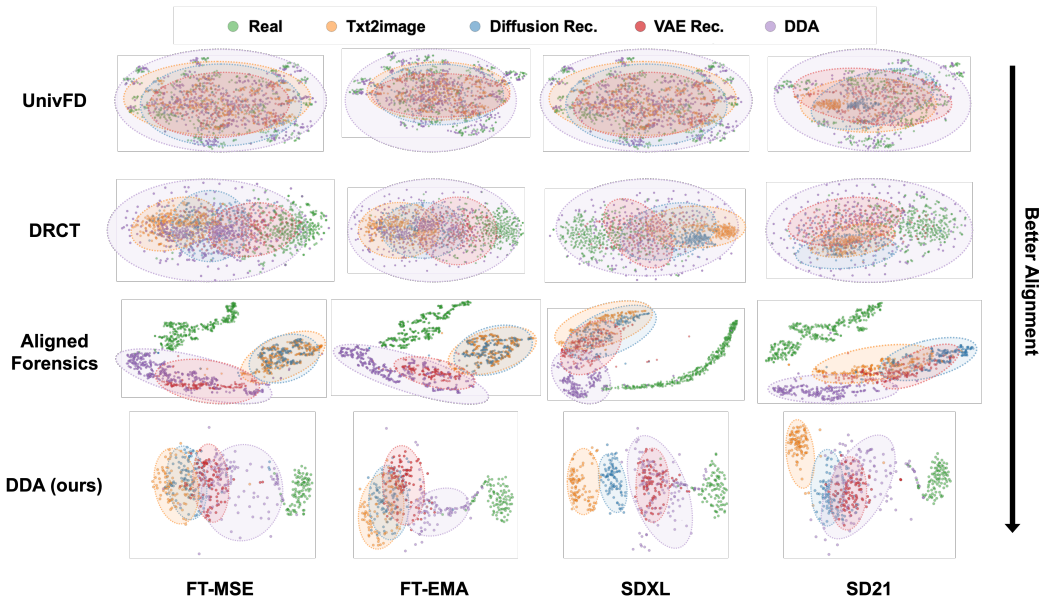


Figure 11: t-SNE visualizations comparing real and synthetic images using detectors trained with different data alignment methods. Rows correspond to the data alignment method used during detector training, while columns represent the generative pipeline—either VAE or diffusion—used to produce synthetic images. **The results show that detectors trained with better dataset alignment are able to separate reconstructed images more distinctly, highlighting the importance of effective dataset alignment in achieving clearer feature space separation.**

in the Appendix. The results clearly demonstrate the superior generalizability of DDA. **DDA achieves an average improvement of 14.2% over the second-best method, while maintaining only 65% of its standard deviation. Its minimum accuracy surpasses that of AlignedForensics—a leading dataset alignment method—by a substantial margin of 20.4%.** These findings indicate that DDA learns truly universal artifacts, capable of transferring across diverse generative models with reduced sensitivity to dataset biases. Notably, AlignedForensics and DRCT rank second and third in minimum accuracy, reinforcing the importance of effective dataset alignment.

**Comparison on AIGCDetectionBenchmark** Table 12 summarizes performance results on the AIGCDetectionBenchmark dataset. **DDA outperforms the second-best detector by 8.5% and**

achieves the lowest standard deviation among all methods that surpass a 70% average balanced accuracy.

**Comparison on ForenSynth** Table 13 presents results on ForenSynth, which comprises images from 11 GAN models. The top two methods—C2P-CLIP and FatFormer—were trained on ProGAN data originating from the same domain as ForenSynth. **In contrast, DDA is trained exclusively on VAE-reconstructed images and has never seen GAN-generated content during training. Nevertheless, it achieves an impressive 85.5% accuracy on ForenSynth, demonstrating strong cross-generator generalizability.**

**Detailed Comparison with B-Free [13]** Table 14 compares DDA with B-Free on the Synthbuster and WildRF datasets. **DDA achieves the highest accuracy on both, outperforming B-Free by 0.9% on Synthbuster and 1.8% on WildRF. It also records the lowest standard deviation—approximately one-seventh that of B-Free—indicating more stable performance. Moreover, DDA requires only about 0.25% of the training data generation cost reported for B-Free, as described in main paper Section 4.** These results underscore DDA’s effectiveness and practicality for scalable deployment.

**Comparison to Dataset Alignment Methods in Feature Domain** Fig 11 presents t-SNE visualizations of real and synthetic image features, generated by detectors trained with varying data alignment strategies. Each row, from top to bottom, represents detectors trained on datasets with progressively stronger alignment. **Detectors trained on better-aligned datasets yield more separable feature distributions, suggesting that enhanced alignment facilitates clearer decision boundaries between real and synthetic content.** These findings reinforce the role of data alignment in improving feature separability and overall AGI detector performance.

## D More Ablation Results

**Ablation on VAE** Table 15 presents the performance of detectors trained on data reconstructed by different VAEs. The results show **broadly comparable performance across most VAEs**, suggesting the presence of universal artifacts inherent in VAE-based reconstructions that are effectively learned by the detector. Notably, training on combined datasets reconstructed from multiple VAEs does not significantly improve accuracy. This may be because each VAE introduces similar synthetic artifacts, meaning that additional VAE-reconstructed images do not contribute novel information. Detectors trained on data reconstructed using the VAE from SD3.5 exhibit lower performance. We hypothesize that this is due to the VAE from SD3.5 introducing reconstruction patterns that differ structurally from those of other VAEs.

**Ablation on Input Size** Table 16 presents an ablation study of our method across different input sizes, ranging from 224 to 504. Detectors achieve comparable accuracies across these input sizes.

**Ablation on Backbone** Table 17 presents an ablation study comparing the performance of different backbone architectures. The ResNet backbone is excluded from this study due to training instability and failure to converge. The relatively poor performance of linear probing methods is attributed to the limited representational capacity of a single linear layer. This observation aligns with the convergence issues observed with ResNet, suggesting that the universal artifacts in our training data are inherently more difficult to learn. In contrast, AlignedForensics [27] successfully employs a ResNet backbone, implying that the artifacts used in our training setup may be subtler or more complex than those captured in prior work. Another key finding is that DINO-LoRA outperforms CLIP-LoRA by a margin of 7.3%. This performance difference is likely due to the architectural focus of each backbone: CLIP emphasizes high-level semantic features, while DINO is more attuned to low-level visual patterns—which are more indicative of AI-generated image artifacts. Moreover, DINO-LoRA achieves a lower standard deviation, indicating greater stability during training and reinforcing its suitability as a backbone for robust AGI detection.

```
Prompt 00 a photo of a backpack
Prompt 01 a photo of a backpack below a cake
Prompt 02 a photo of a backpack right of a sandwich
Prompt 03 a photo of a banana
Prompt 04 a photo of a baseball bat
Prompt 05 a photo of a baseball bat and a bear
Prompt 06 a photo of a baseball bat and a fork
Prompt 07 a photo of a baseball bat and a giraffe
Prompt 08 a photo of a baseball glove
Prompt 09 a photo of a baseball glove and a carrot
Prompt 10 a photo of a baseball glove below an umbrella
Prompt 11 a photo of a baseball glove right of a bear
Prompt 12 a photo of a bear
Prompt 13 a photo of a bear above a clock
Prompt 14 a photo of a bear above a spoon
Prompt 15 a photo of a bed
Prompt 16 a photo of a bed right of a frisbee
Prompt 17 a photo of a bed right of a sports ball
Prompt 18 a photo of a bench
Prompt 19 a photo of a bench and a snowboard
...
```

## E More Details of EvalGEN

To construct EvalGEN, we use 553 distinct prompts, each of which generates 20 synthetic images per generator, resulting in 11,060 images per generator. This results in a total of 55,300 synthetic images in the complete EvalGEN dataset. All images are stored in JPEG format with quality factor 96. A subset of these prompts is provided above to demonstrate the dataset’s diversity and semantic coverage, and Fig 12 demonstrates some visual examples of our EvalGEN dataset.

## F Regional Detection Analysis

Figure 13 displays heatmaps of detection scores across segmented image regions, with numerical overlays indicating the detector’s predictions. These results reveal that detection scores vary by region, indicating that synthetic artifacts are spatially uneven. This observation suggests that localized detection strategies could further enhance robustness.

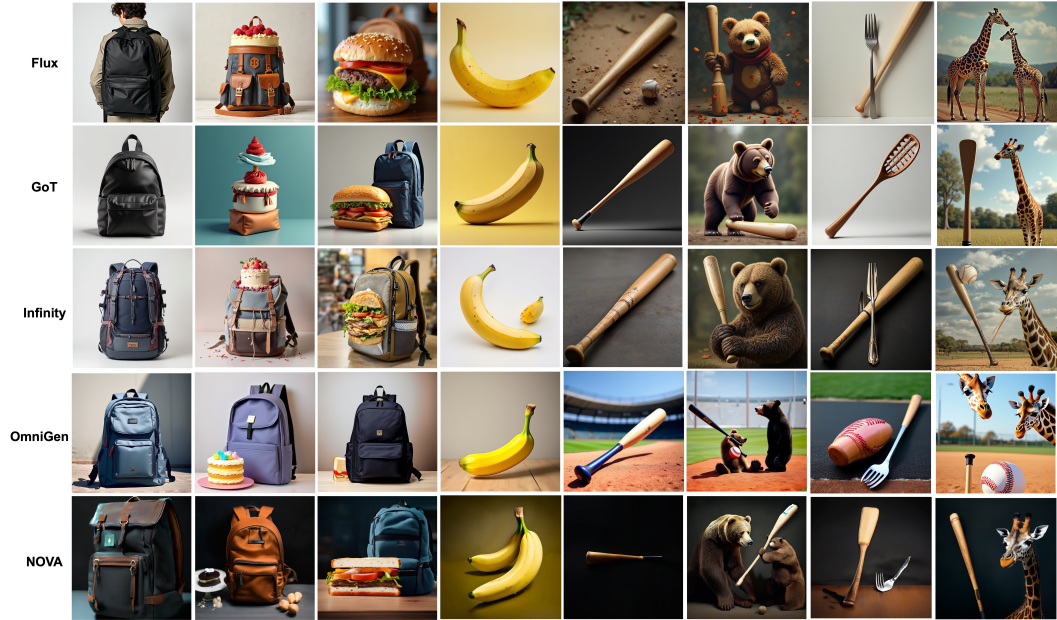


Figure 12: Examples from EvalGEN.

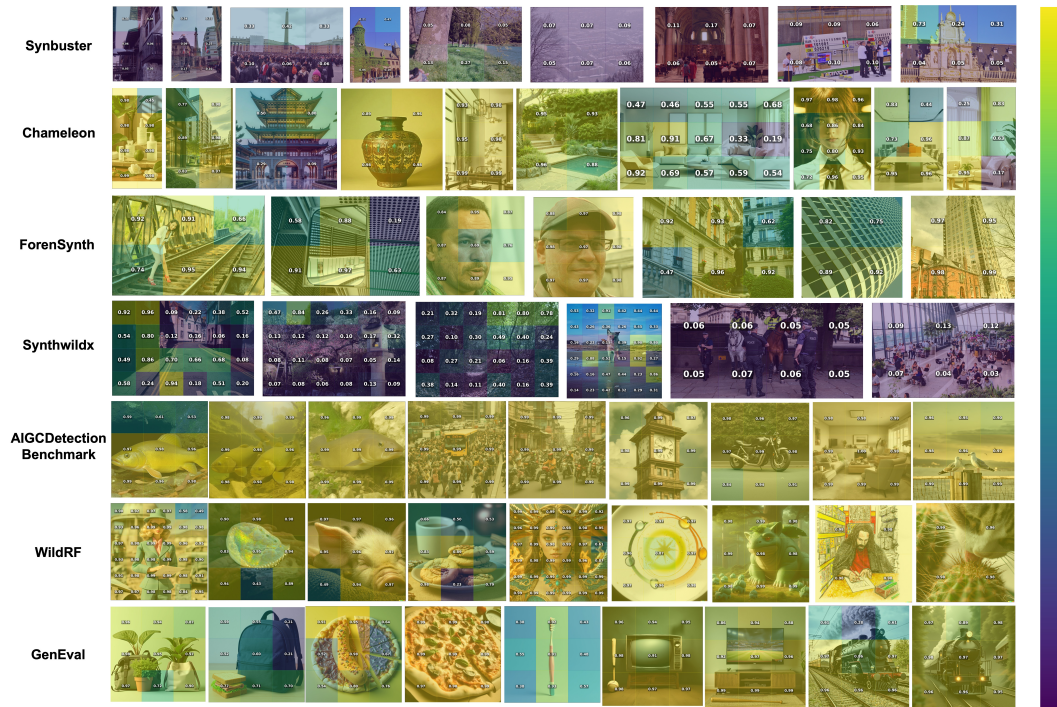


Figure 13: Results of patch evaluation from various datasets.